Fuel 324 (2022) 124768

Contents lists available at ScienceDirect

Fuel

journal homepage: www.elsevier.com/locate/fuel

Full length article

A numerical investigation of the performance of oxymethylene ethers blended with fossil diesel to reduce soot emissions in compression ignition engines

José M. García-Oliver, Ricardo Novella, Carlos Micó *, Usama Bin-Khalid

CMT - Motores Térmicos, Universitat Politècnica de València, Camino de Vera s/n, 46022 Valencia, Spain

ARTICLE INFO

Keywords:
Computational fluid dynamics
Compression ignition
Oxymethylene ether
E-fuels
Soot

ABSTRACT

The reduction of the carbon footprint of internal combustion engines and the pollutant emissions is mandatory for the survival of this technology. In this sense, e-fuels are considered as a potential pathway to achieve this reduction and even remarkable carbon footprint mitigation in compression ignition engines. Among numerous e-fuels, oxymethylene ethers stand out because of their low soot formation characteristics. However, the complexity of their physical and chemical properties makes it a challenge to be used in conventional engines. The aim of the current study is to investigate the effects of the stoichiometry of oxymethylene ether on the in-cylinder combustion behaviour and the pollutant formation when blended with fossil diesel. For this purpose, numerical simulations of a medium duty optical engine fuelled with these blends were carried out using CONVERGE CFD, which were validated with experimental data. Different reaction mechanisms that can be found in the literature were evaluated, using n-heptane as to the fossil diesel surrogate and OME_3 as the oxymethylene ether surrogate. Results highlight the differences in terms of equivalence ratio fields achieved when varying the e-fuel content in the blend. As a consequence, the combustion process is faster and the soot formation is drastically reduced when the oxymethylene ethers content is above 30%. This makes these blends interesting to reduce the well-known soot-NO_x trade off of compression ignition engines.

1. Introduction

The contribution of the transport sector to the greenhouse effect and global warming is well known. It has been reported that the transportation sector is responsible for almost 18% of total CO_2 emitted in energy sector in european union (EU) [1] while heavy duty vehicles contribute with more than 25% of the total EU green house gas (GHG) emissions from road transport sector [2]. On top of that, diesel operated vehicles have additional significant emissions-related problems, due to their well known soot-NO_x trade off [3]. Besides, studies reveal that the direct vehicle emissions related to particulate matter are predominantly generated by diesel vehicles [4]. For this reason, increasingly restrictive regulations are put in place to limit the environmental impact. To face this situation, a great amount of research is being carried out and different pathways have been defined. In the last years, the implementation of hybridization and electrification in power trains [5] has gained lot of attention. Even most of the main automotive manufactures have chosen this approach to achieve the desired emission reduction. However, for certain applications (heavy duty) or in certain markets the electrification is not applicable in short or medium term. In these scenarios, the internal combustion engines will still play a major role and the use of renewable fuels to replace the conventional ones will allow to achieve a reduction of fossil fuel dependency and cleaner combustion [6]. These fuels are manufactured by using renewable energy. In fact, they are considered as ways of renewable energy storage and transportation. They can be bio-fuels [7] if they are produced from biomass or synthetic fuels, also known as e-fuels [8]. Focusing on the last ones, they are considered a promising alternative to drastically reduce engines carbon footprint and even achieve carbon neutrality [6]. Primarily these fuels are produced from electrolysis of water, converting this molecule into their individual components (H_2 and O_2) [9], and from carbon capture for obtaining CO_2 [10] that is later used as the carbon source for e-fuels production. The use of CO_2 for its production as well as renewable energy sources contribute to reduce its carbon footprint and to achieve carbon neutrality [8].

Among the e-fuels category, dimethyl ether containing oxymethylene groups (OME_x) also termed as polyoxymethylene dimethyl ether (PODE) have been widely considered as an interesting alternative to fossil diesel due to their very low soot formation during the combustion

* Corresponding author.
E-mail address: carmirec@mot.upv.es (C. Micó).

https://doi.org/10.1016/j.fuel.2022.124768
Received 29 March 2022; Received in revised form 19 May 2022; Accepted 2 June 2022
Available online 14 June 2022

Abbreviations

AMR	Adaptive mesh refinement
CAD	Crank angle degree
CFD	Computational fluid dynamics
CI	Compression Ignition
CN	Cetane number
CO	Carbon monooxide
CO_2	Carbon dioxide
D100	100% Diesel in mass
D50O50	50% Diesel - 50% OME_x in mass
D70O30	70% Diesel - 30% OME_x in mass
D80O20	80% Diesel - 20% OME_x in mass
D90O10	90% Diesel - 10% OME_x in mass
DCI	Direct compression ignition
DICI	Direct ignition compression ignition
DMM	Dimethoxymethane
e-fuel	Electrofuel
EGR	Exhaust gas recirculation
EVO	Exhaust valve opening
GHG	Green house gas
H_2	Hydrogen molecule
HCCI	Homogeneous charged compression ignition
HRR	Heat release rate
ID	Ignition delay
IVC	Intake valve closing
LHV	Lower heating value
NO_x	Nitrogen oxides
O_2	Oxygen molecule
OH	Hydroxyl radical
OH*	Excited hydroxyl radical
OME	Oxymethylene ether
PAH	Polycyclic aromatic hydrocarbons
PM	Particulate matter
PODE	Polyoxymethylene dimethyl ether
PRF	Primary reference fuel
SOC	Start of combustion
SOE	Start of energizing
SOI	Start of injection
TDC	Top dead centre
TER	Total energy released
TRF	Toluene reference fuel
WDF	Wide distillation fuel
0D	Zero dimensional
3D	Three dimensional
°aTDC	Crank angle degrees after top dead centre
Φ	Equivalence ratio

process [11]. OME_x have a molecular structure of CH_3–O–$(CH_2$–O$)_x$–CH_3 where x ranges from 1 to 6. This fuel has high oxygen content in its molecular composition without any C–C bond, which are the main reasons for low soot formation during combustion [12]. Furthermore, OME_x have a high cetane number (CN), which mainly depends upon the chain length of molecules and which is usually higher than that of fossil diesel. In fact the CN of OME_x exceeds 60 when x is larger than 1 [13]. Moreover the resemblance of the physical properties of OME_x with those of fossil diesel makes it a perfect fuel to be used as a blend with fossil diesel in any ratio [6,14]. So, thanks to these characteristics, OME_x has been of great interest for researchers for the past few years. Numerous detailed experimental studies have reported a significant reduction in soot and PM emissions either using neat OME_x or OME_x blends with fossil diesel [15,16][17]. It has also been reported that this fuel allows to use high rates of exhaust gas recirculation (EGR) to reduce NO_x without penalizing the soot formation, which ultimately leads to the reduction of the soot-NO_x trade off [18]. The life cycle analysis of OME_x presented by Benajes et al. [19] resulted in reduction of well-to-wheel carbon emissions of up to 19% as compared to diesel–gasoline dual fuel mode, mainly due to OME_x production process which requires carbon capture and a clean electric energy source. In addition, Hank et al. [20] presented OME_x as a potential solution to bring down local PM and NO_x emissions.

Nowadays multi-dimensional computational fluid dynamics (CFD) simulations coupled with chemical kinetics have also emerged as a comprehensive tool to be used to deeply understand combustion process [21]. To the authors knowledge, few numerical studies about blends of fossil diesel with OME_x have been carried out in recent years. These studies are mainly focused on the development of the reaction mechanism needed for their simulation, in turn validating their numerical model with an experimental dataset. In 2016, Sun et al. [22] developed a high temperature kinetic mechanism for OME_3 and validated it against experimental results. His study highlighted that, owing to the absence of C–C bonds in the C-O chain structure, a significant reduction of soot was achieved. Later He at al. [23] constructed a detailed mechanism for OME_x combustion for low and medium temperature engine applications. Their results were widely validated against ignition delay data and combustion under HCCI conditions. Following his work, Ren et al. [24] created a reduced OME_x-diesel mechanism. Their work was also validated in terms of ignition delay, flame speed and combustion under HCCI conditions. Further, numerical simulations of a direct injection compression ignition (DICI) engine were also performed, which confirmed that the use of high OME_x content in the blends greatly reduced soot emissions. Lv et al. [25] reported that the more OME_x is added in the blend, the more the air–fuel mixing was promoted, thereby decreasing the soot and carbon monoxide emissions. Recently, Lin et al. [26] developed an OME_x-toulene reference fuel (TRF) mechanism that was used for numerical simulations in both HCCI and light duty DICI engine conditions, confirming a decrease of soot formation when adding OME_x to diesel.

Considering all the above mentioned, a high interest on OME_x as an alternative fuel is justified, for reducing the soot-NO_x trade off as well as the carbon footprint of transport sector. Therefore, the aim of this work is to deepen into understanding how the properties and the molecular structure of OME_x affect the combustion process and pollutant formation of OME_x- fossil diesel blends in a CI engine when the composition is varied within a wide range (from 10 to 50% of OME_x content in the mixture). For this purpose, a direct comparison of different reaction mechanisms from literature was carried out to identify the one that best reproduced the experimental behaviour observed. Then, a detailed 3D numerical study of a CI medium duty optical engine fuelled with those OME_x–fossil diesel blends was performed. The simulations show that the increase of OME_x in the blend has strong impact not only on soot formation but also on combustion development. Small differences are observed when the substitution rate of OME_x is below 20% but, above this percentage, a higher influence of the oxygenated fuel is reported. All results have been corroborated by experimental data from direct visualization of the combustion process in an optical engine used as reference for simulations in this work. One of the main novelties and contributions of this work is the identification of the most suitable mechanism for performing the OME_x-fossil diesel blend simulations under operating conditions similar to those found in a DICI engine. In addition, the use of high-speed visualization as well as experimental thermodynamic engine data to compare with numerical results improves understanding and detail in comparison with previous studies. Furthermore, unlike other related numerical studies, this work

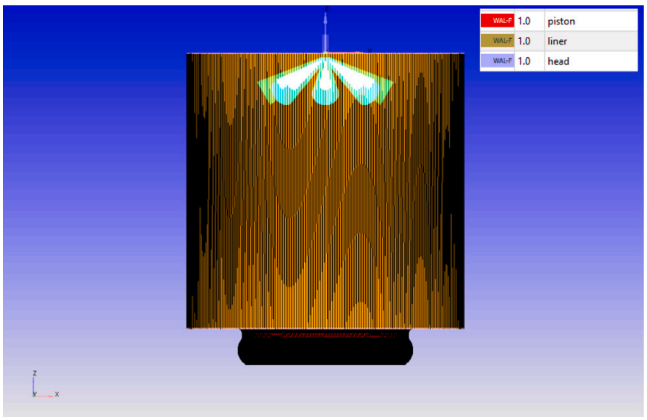

Fig. 1. Computational Domain.

Table 1
Main parameters of the optical engine.

Number of cylinders	1
Bore (mm)	103
Stroke (mm)	99
Displacement (cm^3)	825
Connecting rod length (mm)	163.63
Compression ratio	13.05:1
Engine speed (rpm)	1250
Initial swirl ratio	1.5
Intake valve closing timing (°aTDC)	−148
Exhaust valve opening timing (°aTDC)	115.5

analyses in detail the different stoichiometry of the blends and its impact on the combustion development. Finally, it is worth mentioning that the study was performed on a medium duty CI optical engine, which makes a difference when compared to the HCCI or light duty CI operating conditions that are mostly used in the related literature.

2. Methodology

2.1. Computational domain

Simulations have been carried out using a 3D model of a single cylinder optical engine as computational domain using the commercial CFD code CONVERGE CFD [27]. The geometry is based on a medium duty engine platform (0.8L displacement) used in reference experimental study [12]. The main specifications of the engine are listed in Table 1. The computational domain represents the combustion chamber of the engine that is delimited by the inner piston surface (bowl and squish region), the cylinder liner and the cylinder head plane as shown in Fig. 1.

2.2. Operating conditions

The simulation was run from inlet valve closing (IVC) to exhaust valve opening (EVO). Thus, only compression, combustion and expansion processes were simulated while air management was excluded. An initial swirl ratio of 1.5 was defined to take into account the air movement at IVC. Thermodynamic conditions used to initialize pressure and temperature fields in simulations were obtained from the experimental measurements in the optical engine used here as Ref. [12]. For this purpose, an in house developed zero-dimensional single zone thermodynamic model [28] was utilized. Based on the intake, exhaust and in-cylinder pressures as well as the intake temperature and air mass flow rate, the model is able to calculate in-cylinder thermodynamic conditions at IVC which are later used to define an initial pressure and temperature homogeneous field within the computational domain. The same model was also used to calculate in-cylinder surface temperatures. It uses a nodal model to calculate the liner, piston and the head mean temperatures, which were later used as the boundary conditions for the CFD model. In order to confirm the accuracy of IVC conditions used for the CFD model, the simulation was first run for the motored (no combustion) case.

The Fig. 2(a) shows the in-cylinder pressure comparison between CFD and experimental data between −20 to 20°aTDC; injection and combustion takes place within this range. The Fig. 2(b) represents the in-cylinder temperature evolution comparison. By looking at both pressure and temperature comparisons, it can be seen that simulation was able to simulate the in-cylinder conditions with accuracy.

2.3. Mesh configuration

Before selecting an appropriate mesh size, a mesh sensitivity analysis was performed. It's effect over the heat release rate (HRR) and pressure were used as reference. The basic configuration included a fixed embedding scale of 2 around the nozzles as well as adaptive mesh refinement (AMR). It allowed to automatically refine the grid based on local fluctuations of temperature and velocity with a maximum configured embedding scale of 3. The Table 2 shows the different mesh configurations evaluated, where the main parameter modified was the base grid size.

The results of the mesh sensitivity analysis are shown in Fig. 3. Data corresponds to the simulation of a blend of 50% Diesel and 50% OME_3 (in mass). It can be seen that HRR and pressure are different for the Mesh A when compared to the others, which are much more similar among them. However, with Mesh B still some small discrepancies in comparison to Mesh C and Mesh D are observed. Therefore, it can be concluded that results were almost not affected by the base mesh size when it was lower than 1.5 mm.

Considering this, a base mesh size of 1.25 mm with the fixed embedding and AMR previously described, leads to a minimum grid size of 0.3125 mm. The Fig. 4 shows the mesh within a plane that represents half of the computational domain at 0°aTDC. It is possible to see the effect of AMR and fixed embedding around one of the fuel sprays as well as at some regions close to the walls.

2.4. Chemical mechanism configuration

In this study, different blends of diesel with 10%, 20%, 30% and 50% in mass of OME_x were simulated. From here on they will be identified as D90O10, D80O20, D70O30 and D50O50 respectively. The OME_x fraction in blends was limited up to 50% owing to energy reduction caused by the lower LHV of this fuel which has been already discussed in the literature [12,26]. Due to the complexity of this fuels, surrogates ones were used for simulations instead. For diesel, n-heptane was used as it is a widely accepted as a surrogate for conventional Diesel [29,30]. For OME_x, it must be taken into account that in experiments the fuel was a mixture of different OME chains where x varied from 1 to 6. However, only OME_3 (DMM_3) was used as surrogate in this work. The main reasons for using only one fraction of its composition are two. First, the reaction mechanisms that can be found in literature for this type of fuel blended with others only contains OME_x reaction pathways. Second, this fraction was of the largest one in the OME_x that was used in the reference experimental study [12]. Four different reaction mechanisms for the Diesel–OME_x blends were tested in this work. Their main characteristics are summarized in Table 3.

The first mechanism is the one proposed by He et al. [31]. It is a reduced multicomponent mechanism that was developed for oxygenated wide distillation fuel (WDF) with OME_x. It covers surrogate fuels like n-heptane, iso-octane, OME_3 etc. This mechanism has been previously validated against experimentation in a rapid compression machine, homogeneous charge and direct injection compression ignition (HCCI and DICI) engines. The second mechanism was presented

Table 2
Different Mesh parameters used in Mesh sensitivity analysis.

Mesh type	Mesh A	Mesh B	Mesh C	Mesh D
Base grid size (mm)	2.0	1.5	1.25	1.15
Mesh size around nozzle [Fixed embedding] (mm)	0.5	0.375	0.3125	0.2875
Total number of cells without embedding and AMR	111,664	264,685 (+137%)	457,376 (+310%)	587,367 (+426%)
Computational time	18.5 h	30.5 h (+64.3%)	36 h (+91.9%)	38.5 h (+106%)

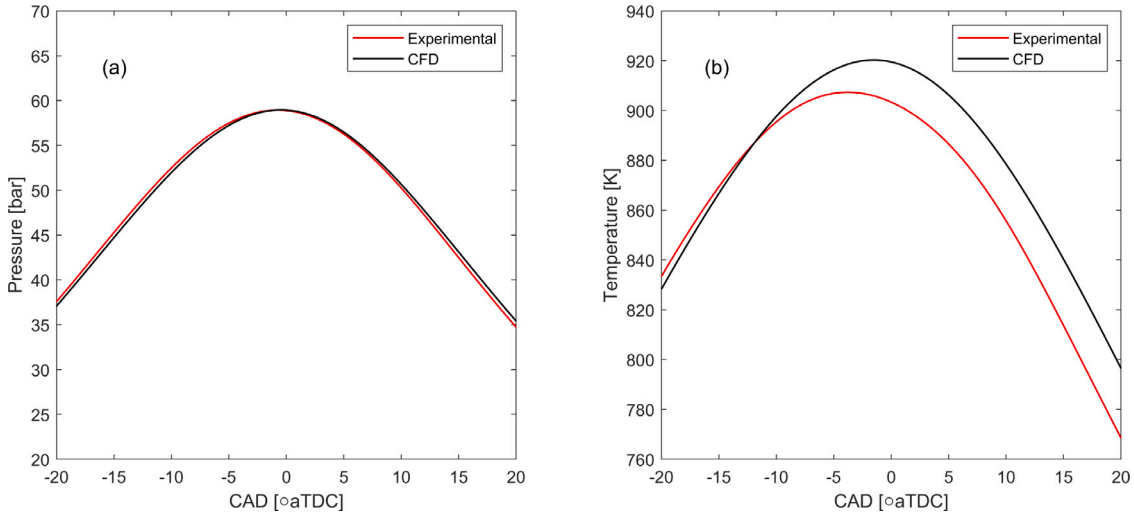

Fig. 2. Numerical and experimental in-cylinder pressure evolution (a) and temperature evolution (b) under motored conditions.

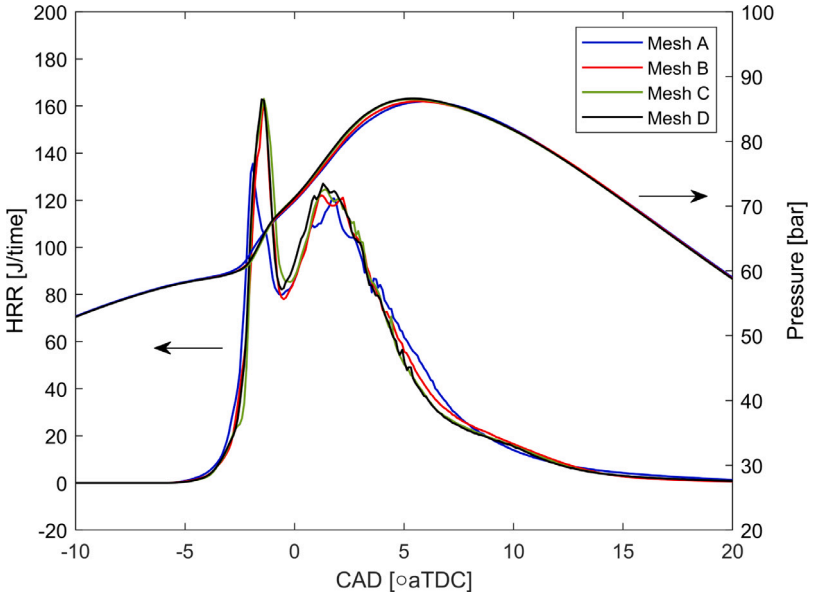

Fig. 3. Mesh sensitivity check for the case of blend of 50% Diesel and 50% OME_3.

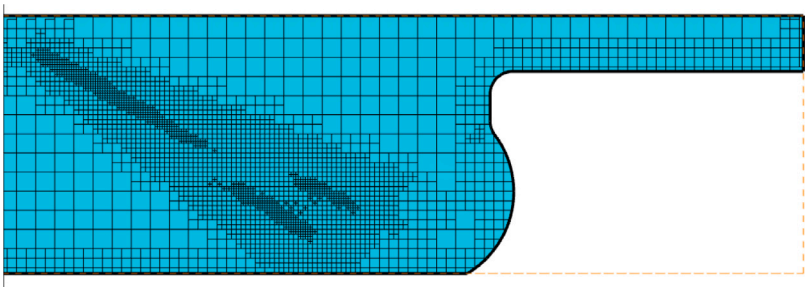

Fig. 4. Mesh distribution at 0°aTDC.

Table 3
Overview of reaction mechanisms used.

Mechanisms	Number of species	Number of reactions	Mechanism type
He 2017 [31]	354	943	WDF-PODE$_n$
Ren 2019 [24]	145	585	PRF-PODE$_n$
Lin 2019 [32]	61	190	PRF-PODE$_3$
Lin 2021 [26]	120	360	TRF-PODE$_3$

Table 4
Main injection spray parameters.

Start of Energizing (SOE) (°aTDC)	−9
Start of Injection (SOI) (°aTDC)	−6.804
Injection duration (°)	8.685
Injection profile	Single main injection
Injection Pressure (bar)	1000
Number of nozzles	1
Number of holes in nozzle	8
Discharge co-efficient	0.9
Orifice diameter (μm)	135
Spray cone angle (°)	14
Angle between spray axis and cylinder head (-zx plane) (°)	60

by Ren et al. [24]. It is a reduced primary reference fuel (PRF)-OME$_x$ chemical mechanism and has been extensively validated in a HCCI engine. The third mechanism considered in this study is a (PRF)-OME$_x$ compact mechanism, proposed by Lin et al. [32] and extensively validated against a wide range of experimental data. The fourth and last mechanism was recently published by the same authors [26]. The main difference with the previous one is that it is a toluene reference fuel (TRF)-OME$_x$ mechanism that contains TRF-polycyclic aromatic hydrocarbons (PAH) chemistry, essential for soot predictions. It has also been validated against a range of experimental and simulation results.

2.5. Injector configuration

In this simulation, an injector with 8-hole nozzle was used. The start of energizing (SOE) was set at −9°aTDC for every case with a start of injection (SOI) delayed about 2.196 CAD from SOE and a total injection duration of 8.685° as it was measured experimentally. The discharge coefficient was kept constant at 0.9 with the orifice diameter of 135 μm. The angle between the cylinder head plane and the spray axis (-zx plane) was set to 60° as it was experimentally measured. The spray cone angle was set to be 14° as obtained by using a correlation from [33], where this parameter is calculated by an empirically derived equation for a vaporizing spray using the values of the ambient gas density, ambient fuel density and a constant equal to 0.26. Main spray injection parameters used are shown in the Table 4.

The injected mass flow rate was experimentally measured for D100 (corresponding to 100% pure diesel) and D50050 at 1000 bar injection pressure with the energizing pulse of 900 μs, as in reference experiments, following the methodology described in [12]. Both injection rate profiles have been presented in Fig. 5.

As it can be observed, the main effects when increasing the OME$_x$ content is that the instantaneous mass flow rate increased while its duration was slightly shortened (2% of total duration). These resulted in a noticeable increase of the total injected mass when increasing the OME$_x$ content. Liu et al. [34] reported a reduction of the viscosity of similar blends when increasing this fuel fraction, which could be the reason after the progressive increase of injection rate observed here. For sake of simplification, it was decided to use the D50O50 normalized injection rate profile for all the fuels. However, to take into account the described behaviour, the corresponding measured total injected mass was used for D50O50 while a different value was calculated for D90O10, D80O20 and D70O30 (as no measured values were available).

For this purpose, a linear relation between OME$_x$ content and total injected mass variation was assumed and the values corresponding

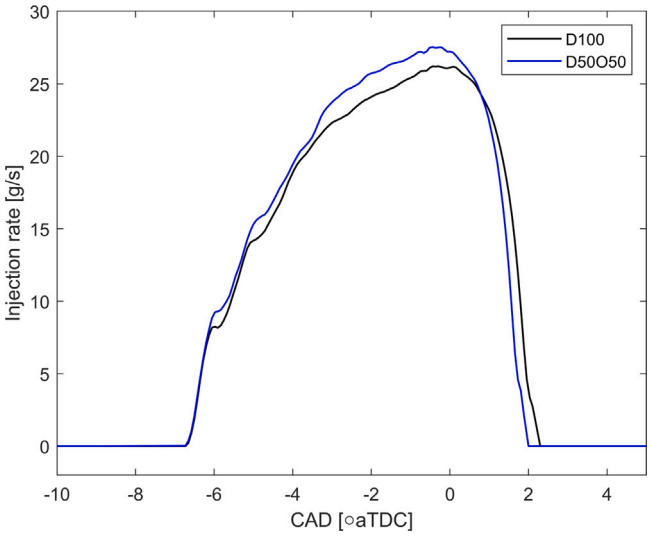

Fig. 5. Mass flow rate for D100 and D50O50 case.

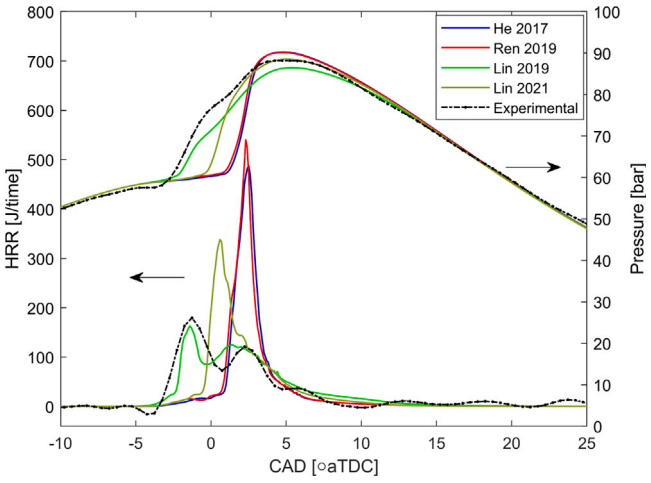

Fig. 6. Experimental data and different mechanisms simulations (CFD) of pressure profile and heat release rate for D50O50.

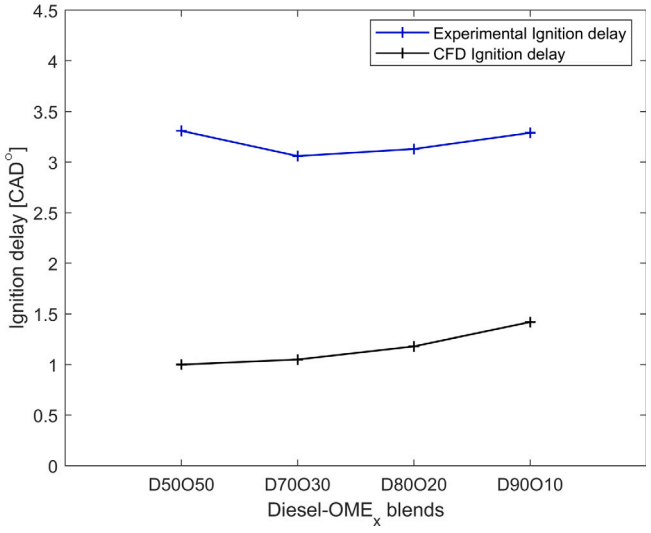

Fig. 7. Both experimental and CFD ignition delay.

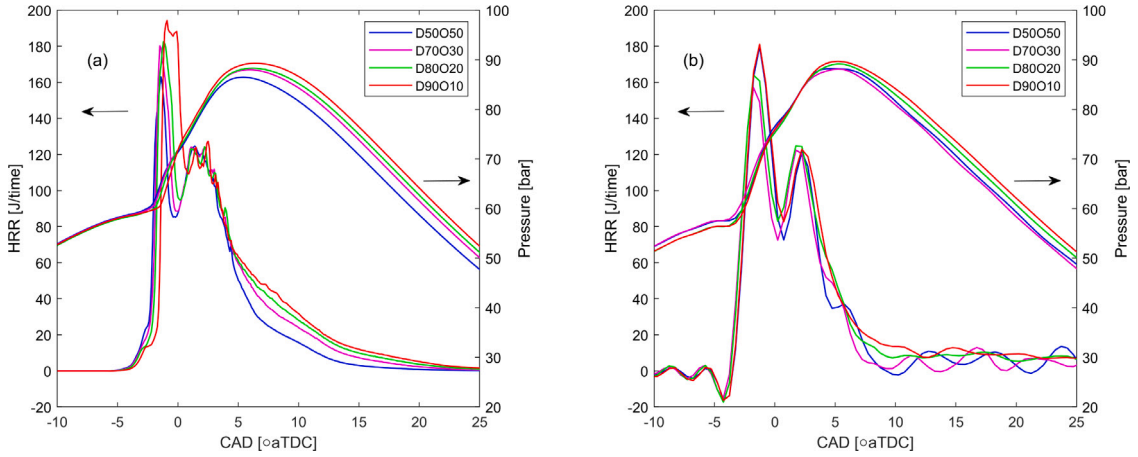

Fig. 8. In-cylinder pressure and heat release rate obtained from numerical simulations (a) and from experimental results reproduced from [12] (b).

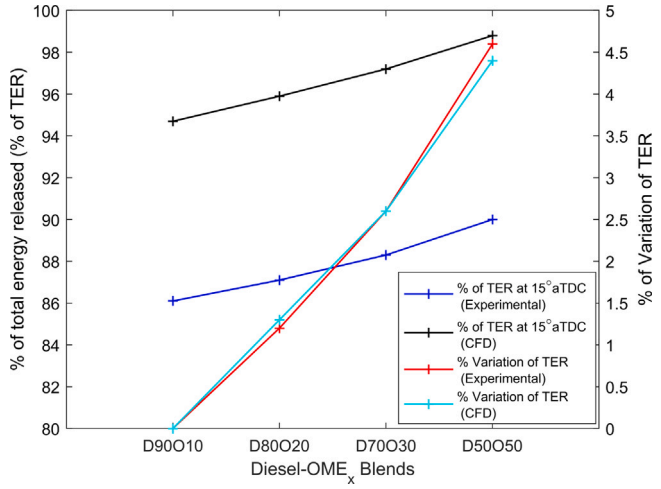

Fig. 9. Numerical vs experimental percentage of total energy released (TER) at 15°aTDC for each blend and the percentage variation of this parameter w.r.t D90O10 results.

Table 5
Injected mass for each blended fuel.

Blend	Total injected mass (mg)
D50O50	32.22
D70O30	31.44
D80O20	31.05
D90O10	30.66

to 10%, 20% and 30% of this fuel were calculated using a linear interpolation procedure. The total injected mass calculated for each fuel is summarized in Table 5.

2.6. Spray and combustion models configuration

In CI engines, the liquid fuel is injected near the end of compression stroke inside the combustion chamber. So, after injection, the fuel spray undergoes numerous processes like atomization, vaporization etc. There are numerous models available for each phenomenon in the CONVERGE CFD library to handle these phenomena. The Table 6 shows a summary of the ones used in this work.

The liquid injection model employed here was blob injection model [27] that simply depicts the parcels that are injected inside the computational domain with a characteristic size equal to the size of the nozzle diameter. The spray model used here is based on lagrangian drop eulerian type and the modified Kelvin–Helmholtz Rayleigh–Taylor (Modified KH-RT) was used as a spray breakup model [27]. In this model the primary breakup of injected liquid blobs is due to the aerodynamic instabilities. During this process child drops are formed and the secondary breakup of these drops is modelled by assessing the competing effects of KH and RT Mechanisms. The droplet collision was based on No time counter (NTC) model by Schmitz and Rutland [27]. This method involves the randomly determined sub sampling of the parcels within each cell that results in much faster collision calculations. Finally, a rebound/slide model was used to model the spray wall interaction. All these spray models described are well used in literature and are recommended by CONVERGE for diesel engine simulations.

Table 6
Different spray models used.

Liquid injection	Blob injection
Spray breakup	Modified KH-RT
Drop Drag	Dynamic Drag Model
Collision Outcome models	Post collision outcome
Turbulent dispersion	O'Rourke model
Collision Model	No time counter (NTC) collision
Spray/wall interaction model	Rebound/slide

The Re-normalization group (RNG) k-epsilon was used to resolve turbulence, with a standard wall function. The renormalized model is more robust than the standard k-epsilon. The effect of turbulence interaction and spray compressibility is included in this model. Turbulent kinetic energy and turbulent dissipation values were provided accordingly. The heat transfer in this simulation was modelled by O'Rourke and Amsden [35,36] model. Navier stokes solver scheme PISO [37], i.e. pressure implicit with splitting of operators, density-based scheme was utilized. Besides, variable time-step scheme was used, that describes each time-step within a pre-defined interval (from $1{\cdot}10^{-8}$ to $1{\cdot}10^{-4}$) based on the maximum number of iterations allowed for the governing equations and the iterative solver, the maximum Courant–Friedrichs–Lewy (CFL) numbers and other restrictions related with sub-models like the spray model [27].

Regarding the combustion modelling, CONVERGE contains a detailed chemistry solver named SAGE [38] that solves the detailed chemical kinetic through the CHEMKIN formatted input files on each computational cell. SAGE solver calculates the elementary reaction rate while CONVERGE solves the transport equations. It happens to provide accurate results in terms of diesel combustion. Moreover, Hiroysou soot model was used in terms of soot modelling in this study.

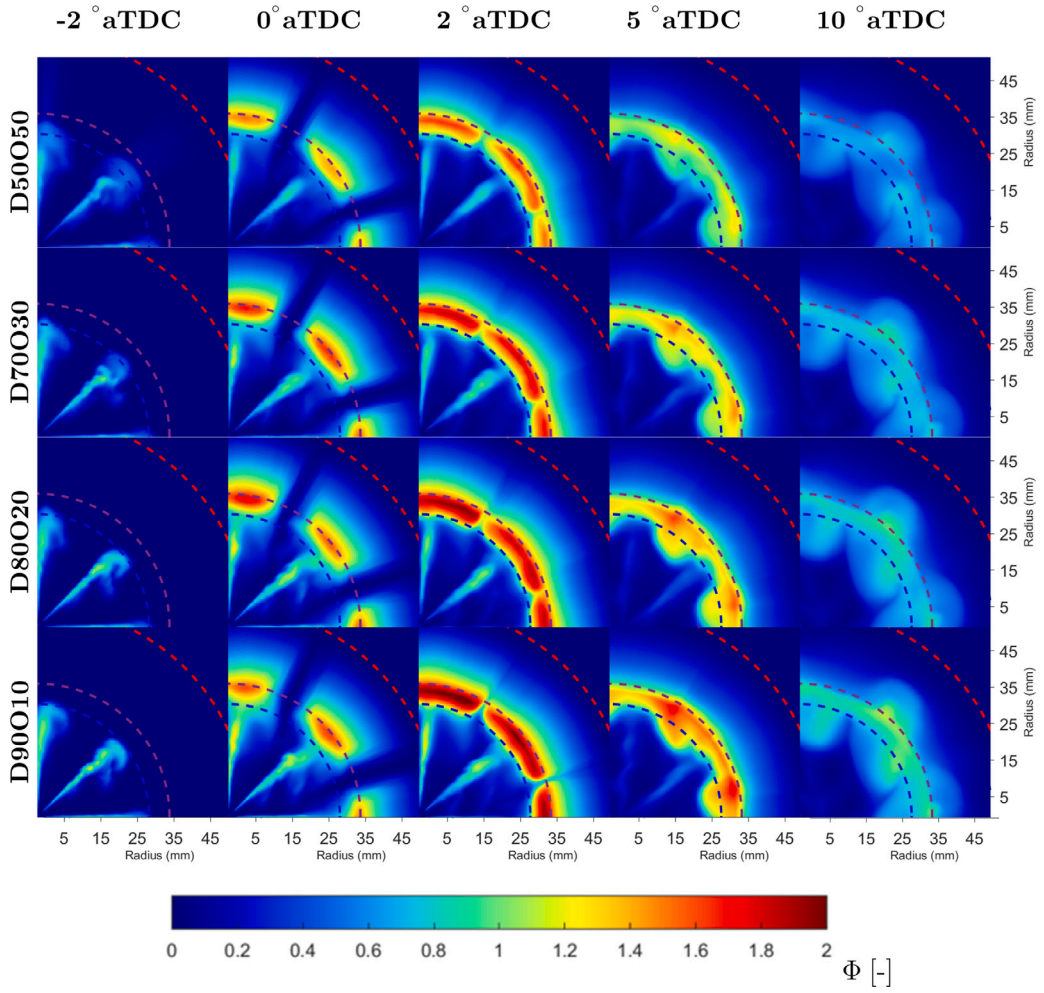

Fig. 10. Average equivalence ratio distribution inside the combustion chamber for the four blends. Data corresponds to numerical simulations.

3. Results and discussion

3.1. Evaluation of reaction mechanisms

Discussion starts by evaluating the comparison of the different reaction mechanisms considered in this study. For this purpose, HRR and in-cylinder pressure signal for D50O50 have been compared with the reference experimental data. The Fig. 6 shows the HRR and pressure curves obtained by using the four mechanisms and their comparison with the experimentally obtained curves.

It is possible to see that only one of the four mechanisms was able to predict a similar behaviour as of experimental data, which is the compact mechanism provided by Lin et al. [32]. It is able to reproduce a similar ignition delay as well as premixed and diffusion phases of the experiments. The longer mechanisms in terms of number of reactions, i.e. [24,31], show a quite similar behaviour between themselves. They predict a longer ignition delay than experiments which results in a more intense premixed phase and almost no diffusion. The mechanism provided by Lin et al. [26] in 2021 also exhibits a longer ignition delay with a more intense premixed phase than experiments. The accuracy on reproducing ignition delay by the Lin 2019 mechanism [32] was also observed by Hovden et al. [39], where the authors performed 0D simulations in a constant volume reactor for ignition delay calculations. Thus, this mechanism was chosen to carry out further simulations in this study.

3.2. Effect of fuel composition on combustion performance and energy release

When analysing the effect of the blend composition on the combustion process development, differences start to appear since the start of combustion. The Fig. 7 shows the ignition delay (ID) obtained both from experimental data and numerical simulations. It has been calculated as the delay between the SOI and the first instant when the HRR goes above 0. It is possible to see that ID slightly increases when OME_x content in blend is decreased. Despite the difference of 2° between both data sources, it can be stated that the trend obtained with the numerical simulations regarding the fuel composition is corroborated by experiments. This behaviour could be related with the fact that as OME_x content is decreased in blend, the oxygen supplied by the fuel itself also decreases making the blend less reactive and delaying combustion. A similar influence of the OME_x fraction over ignitability of the blends was reported by Liu et al. [34], who reported a reduction of the cetane number of the blends as this fraction decreased. However, the relation between ID variation and OME_x content is not linear. Above 20%, ID tends asymptotically to a value close to that shown by D50O50, which suggest that for such blends the most reactive component (OME_x) is controlling the start of combustion [40] and diesel has almost no influence. The same trend can be observed in experiments except for D50O50, which will be analysed in more detail in the following paragraphs.

The results obtained with the selected mechanism for the four blends related to the in-cylinder heat release rate and pressure evolution are compared in Fig. 8. In general, numerical simulations are able

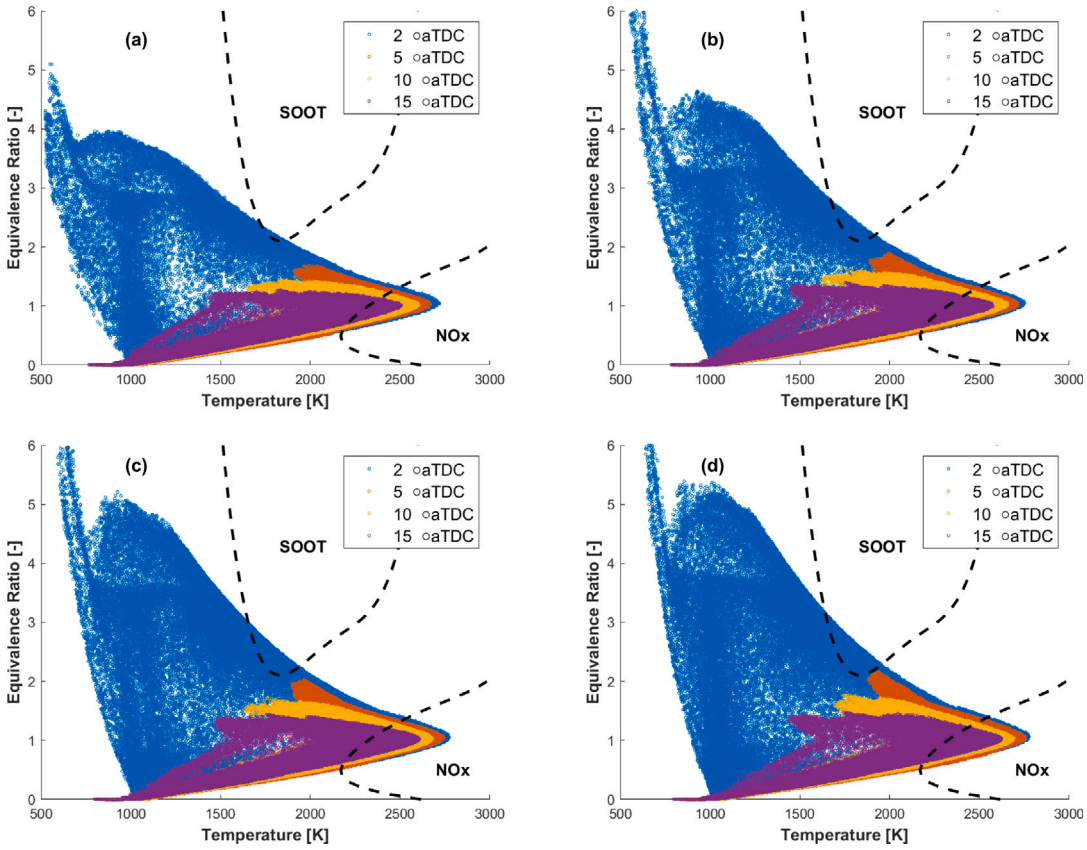

Fig. 11. Equivalence ratio vs temperature distribution for D50O50 (a), D70O30 (b), D80O20 (c) and D90O10 (d) at different instants. Data corresponds to numerical simulations.

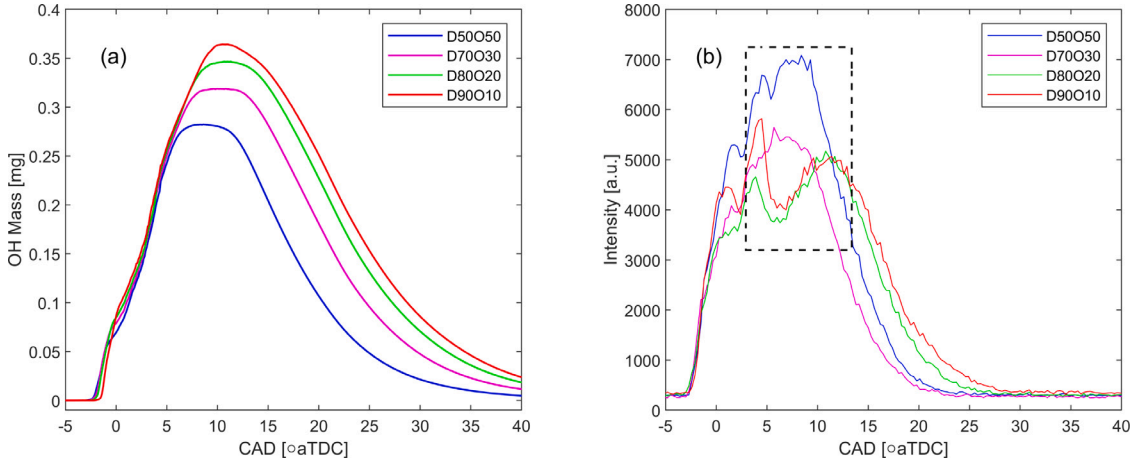

Fig. 12. In-cylinder accumulated OH mass from numerical simulations (a) and experimental accumulated OH* radiation (b) for all the blends.

to predict similar trends as those observed in experiments. However, it is important to mention that experimental D5050 deviates from them showing a similar energy release as D90O10 (and also a ID higher than expected). This has been related to experimental errors since this behaviour cannot be explained by the fuel properties. When comparing the different blends, the effect of its composition starts to be visible when the premixed combustion phase is taking place (between −3° and 0°aTDC). The HRR maximum peak decreases when increasing the OME_x content in the blend. On one hand, this can be related to the fact that the LHV of this fuel is lower than that of pure diesel and, therefore, the energy released by each blend at this stage will be different. In this sense, the increase in the injected mass previously reported seems to not be enough to compensate the energy difference. On the other hand, the ID has an impact on the amount of fuel that mixes with air before combustion and, as a consequence, the energy released in the premixed phase. Thus, the higher ID observed when decreasing the OME_x content is coherent with the more intense HRR peak observed in both CFD and experimental data. Moving further into the diffusion stage, it can be observed that all the fuels present a similar HRR. However, after 5°aTDC the decrease of energy release is more abrupt for the blends with higher OME_x content. This is especially visible when comparing D50O50 and D70O30 with the other two blends and suggest a faster late oxidation stage. This behaviour is clearly visible for the numerical simulation results and is corroborated by experiments, despite the larger oscillations the discrepancies observed for D50O50 as it was previously mentioned.

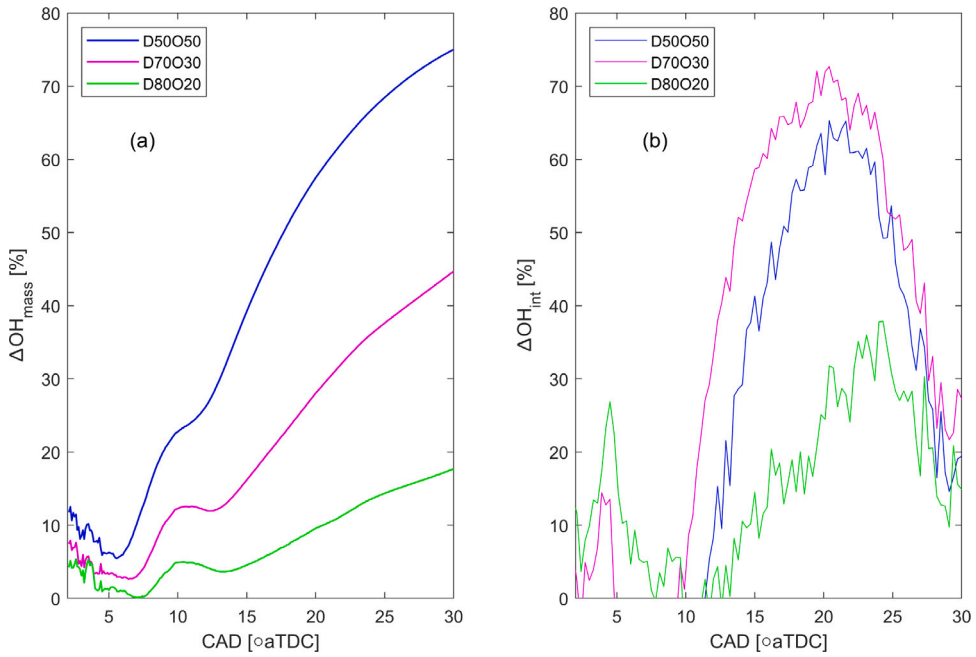

Fig. 13. % Decrease in CFD OH mass w.r.t D90O10 (a) and % Decrease in experimental OH intensity w.r.t D90O10 (b).

At this point, a strategy was defined to quantify how fast combustion is progressing with each blend with respect to D90O10, chosen as reference. The fraction of energy released at 15°aTDC from the total energy released at the end of combustion was calculated, to evaluate how far combustion was completed . This instant was chosen as reference, since it corresponds to the late stages of combustion. The Fig. 9 shows a comparison of the experimental and numerical data, including the percentage of total energy released (TER) for each fuel at 15°aTDC as well as the percentage of its variation with respect to the reference case (D90O10). It can be seen that the percentage of energy released is higher for the case of the largest OME_x fraction and decreases when OME_x fraction is decreased. In fact, by looking at the percentage of variation, D50O50 combustion is almost 5% more complete at 15°aTDC than D90O10. It can be also observed that the trend obtained with CFD is again corroborated by experimental data. Therefore, it can be concluded that combustion is accelerated when increasing the OME_x fraction in the blend.

3.3. Equivalence ratio, temperature and OH distributions

One of the main differences of OME_x when compared to fossil diesel is its molecular composition, which will affect the stoichiometry of the air/fuel mixture and will have an impact on the combustion process. Thus, to get a deeper insight into stoichiometry of the blends, the spatial distribution of equivalence ratio (Φ) inside the combustion chamber is shown in Fig. 10. The data corresponds to the average equivalence ratio calculated between the piston and cylinder head. Besides, it is worth mentioning that Φ in this case do not consider CO_2 and H_2O. It is preferred in this case over the overall equivalence ratio because it can be related with the progress of the reaction [27]. The inner dotted line in the figure represents the field of view of experimental OH* chemiluminescence visualization presented in [12], the middle one represents the bowl radius and outer line represents the piston radius. Besides, it has been decided to represent only a quarter of the bowl to match the experimental data available in [12].

In the figure it is possible to see that higher Φ values are located at the periphery of the bowl for all the cases. In general, D50O50 shows lower equivalence ratios than the other blends. In fact, it is possible to see that the more the OME_x is in the blend, the lesser equivalence ratios obtained. At 2°aTDC (the beginning of the diffusion stage), all the blends seem to reach equivalence ratio values above 2, which decrease as the combustion progresses. At 5°aTDC, the differences among blends are significant with D50O50 showing large regions where equivalence ratio was below 1. In contrast, D80O20 and D90O10 still show regions where Φ is close or even above 2. According to Kitamura et al. [41], more soot is likely to be formed in the regions where Φ is higher than 2. So, based on this, it can be expected that the lower Φ fields achieved thanks to the OME_x content in the blend would result in less soot formation.

The Fig. 11 represents the Φ–temperature diagrams for all the blends at different CAD's. Each point corresponds to one of the cells of the computational domain while the dashed lines represents the soot and NO_x peninsulas. Notice that only at 2°aTDC points in the soot peninsula are visible for every case, with D90O10 showing more points in this region than the other blends. This indicates that soot is likely to be formed at around 2°aTDC and the difference is when decreasing the OME_x content as the point cloud seems to be progressively leaving the soot peninsula. When looking at later instants, it is possible to see that an increase of the oxygenated fraction reduces the Φ field. For example, when looking at the 5°aTDC case, it can be observed that D50O50 is not reaching Φ values above 1, while D90O10 exceeds 2. Regarding temperature, it seems that differences are minimum although it has been reported in [25] that the more OME_x content in the blend, the lesser the equivalence ratios (also observed in this work), but the higher the in-cylinder temperature reached.

The OH radical is considered as a good tracer of high-temperature oxidation reactions. Its spatial distribution identifies the regions where oxidation is taking place. For this reason, it has been decided to investigate the evolution of this radical. In a first approach, Fig. 12(a) represents the accumulated OH mass inside the combustion chamber obtained by CFD for each blend. This data should be comparable with the OH* accumulated intensity in Fig. 12(b) presented by Pastor et al. [12]. It is possible to see that until 5°aTDC all the fuels provide a similar amount of OH mass which is corroborated by the OH* radiation. However, differences appear after 5°aTDC when a decrease of the OME_x content in the blend results in an increase of the in-cylinder OH mass. This is observable with the CFD data but not with experiments. In fact, until 15°aTDC, the second source shows a different trend. However, is was stated by the authors of the experimental work that at this stage of combustion (interval delimited by the dotted rectangle)

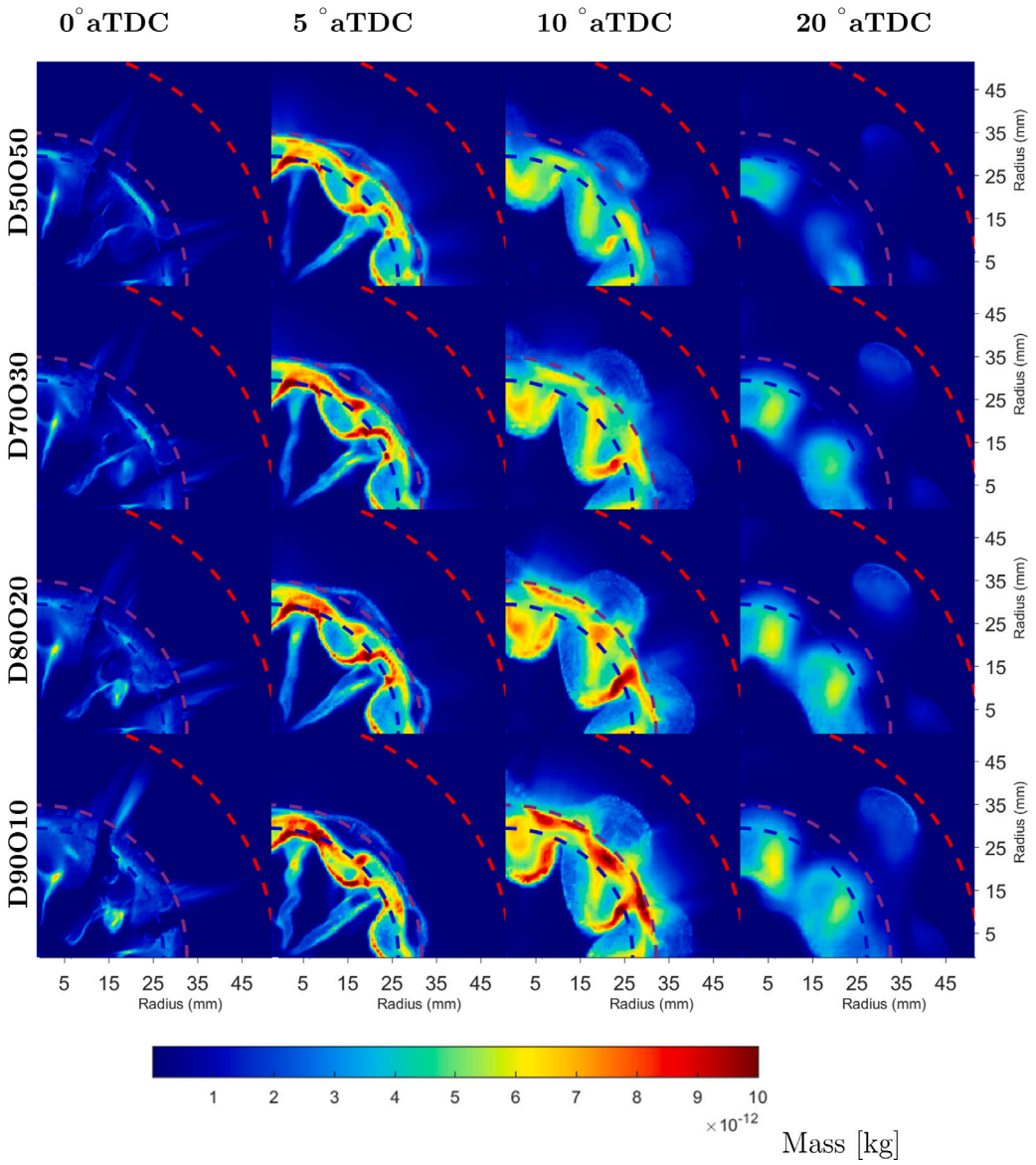

Fig. 14. Accumulated OH mass inside the combustion chamber. Data corresponds to numerical simulations.

the soot peak was reached and the images were contaminated by soot radiation [12]. The OH content starts decreasing earlier for D50O50 and the lesser content of OME_x in the blend seems to delay it more. This results in a sooner disappearance of OH from the combustion chamber, which is coherent with the faster combustion process that was previously mentioned. After 15°aTDC, experimental data provide again a similar trend among the blends as CFD (once soot radiation is not so intense) showing a sooner decay of the signal when the OME_x content is increased. Only experimental D50O50 shows a different behaviour, which has been already discussed in the previous section.

The differences observed in Fig. 12 have been quantified by calculating the percentage of decrease of CFD in-cylinder OH mass (ΔOH_{mass}) and experimental OH intensity (ΔOH_{int}) for all the blends with respect to D90O10. This parameter was calculated as described in Eqs. (1) and (2):

$$\Delta OH_{mass\_X}(\%) = \frac{OH_{mass\_D90O10} - OH_{mass\_X}}{OH_{mass\_D90O10}}.100 \quad (1)$$

$$\Delta OH_{int\_X}(\%) = \frac{OH_{int\_D90O10} - OH_{int\_X}}{OH_{int\_D90O10}}.100 \quad (2)$$

Where X refers to each of the other blends. Results are represented in Fig. 13. Setting aside the soot contaminated region in experimental data, similarities can be observed between CFD and experiments. For D80O20 similar variations are observed (around 20%) while for D70O30 a larger reduction in radiation was obtained (up to 60%) compared with the CFD in-cylinder OH mass variation (up to 40%). These discrepancies could be related with the fact that both magnitudes are not representing the same. Chemiluminescent radiation only comes from excited state radicals which have a very short lifespan. This is especially critical at late stages of combustion where more OH is consumed than formed. However, it can be still concluded from both data sources that larger reductions of OH (or OH*) are observed when increasing OME_x fraction above 20%.

To analyse in more detail how the OH radical is distributed within the combustion chamber, Fig. 14 represents the spatial distribution of this radical obtained with numerical simulations. The represented data corresponds to the accumulated OH mass between the piston and the head surfaces, for all the blends at different instants. Notice that here again only a quarter of the combustion chamber has been represented to match the field of view reported in [12]. The inner dashed line represents the limit of the field of view of the OH* chemiluminescence

experimental visualization, the middle dashed line represents the piston bowl radius and the outer dashed line represents the piston radius.

At the first instants, OH seems to be accumulated close to the periphery of the bowl, which was also observed in the OH* chemiluminescence images from [12]. Moving further, at 10°aTDC significant differences start to appear among blends. D50O50 shows spots of lower OH mass close to the bowl wall while this is not observable for the rest of the blends. Besides, in general the OH field of this blend is lower than the rest. This can be related to the different equivalence ratio distributions reported in Fig. 11. Those spots correspond to the regions where Φ was close to 1. The sooner disappearance of OH observed in Fig. 12 is also visible here.

At 20°aTDC, the major part of OH has disappeared for D50O50 and only small isolated clouds remain. In contrast, the other blends still show larger clouds of higher OH mass which take longer to disappear. For these fuels, the OH clouds seem to evolve from regions where Φ reached the higher values in previous instants, e.g. 5°aTDC. However, for D50O50 they seem to evolve from regions where Φ was significantly below 1.

Considering all the above mentioned, there is a relation between the blend composition, the Φ distribution and the OH distribution. The more OME_x in the blend results in a lower Φ field, thanks to its different stoichiometry (the oxygen content). D90O10, D80O20 and D70O30 provided regions of Φ close or higher than 2 even at 5°aTDC. However, at this stage for D50O50 Φ is lower and closer to 1. This promotes more oxidation in comparison with the other blends, which result in a faster combustion completion (see Figs. 8 and 9) and a sooner OH disappearance.

3.4. Soot formation

As it has been already mentioned in the previous paragraphs, the different Φ fields obtained by each blend will have an impact on soot formation.

To analyse this, Fig. 15 shows the net amount of soot formed (a), the amount of soot produced (b), the amount of soot oxidized (c) and its percentage in relation to the total soot produced (d). The net amount of soot formed is the difference between the soot produced and oxidized. As it can be observed, with the increase of OME_x in the blend, the amount of soot produced decreases while the proportion of soot that is being oxidized increases. This agrees with the Φ–T maps presented in Fig. 11, where it was observed that the less OME_x content resulted in a larger number of points within the soot peninsula at 2°aTDC. In fact, this is the instant when the soot production starts to increase faster for the blends with the lower OME_x fraction. Later, at 5°aTDC, the Φ values decrease (see Fig. 11) for all the fuels and the soot production stops and oxidation becomes dominant. The lower Φ field provided by D50O50 allows it to oxidize the soot faster than the other blends as in can be seen in Fig. 15(d). Besides, the results also show that the effectiveness of oxidizing soot increases with the OME_x content which is consistent with the progressive decrease of Φ values observed previously.

The spatial distribution of soot is presented in Fig. 16, where the net soot formed inside the combustion chamber is shown. Data corresponds to the accumulation of soot mass between the piston and the head surface. Only a quarter of the combustion chamber has been represented as in Fig. 14. These distributions show that at the beginning (close to TDC) the soot distribution is similar for all blends. At 2°aTDC differences appear, as stated previously. In all the cases, soot is mainly formed near the bowl walls which correlates with the experimentally obtained high speed natural luminosity images found in [12]. Besides, it corresponds with the regions of higher Φ values in Fig. 10.

The differences among blends are then mostly related to the amount of soot but not with its distribution. When combustion progresses, it can be seen for D70O30, D80O20 and D90O30 that soot clouds move towards the piston centre while this is not visible for D50O50. This can be related to the fact that, due to the air and spray dynamics, the flames

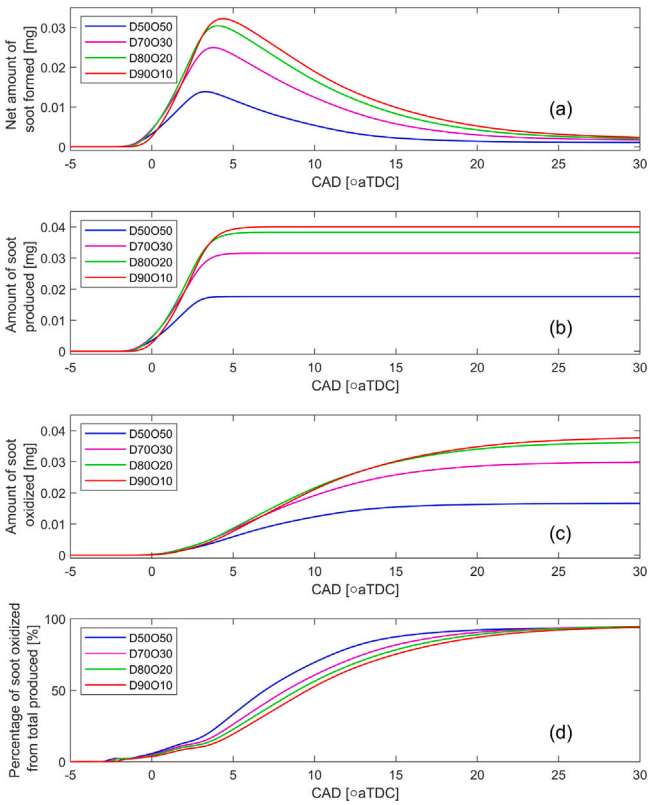

Fig. 15. Evolution of the net amount of soot formed (a), the amount of soot produced (b), the amount of soot oxidized (c), and the percentage of soot oxidized from the total produced (d).

are pushed towards this region. As soot lasts longer when the OME_x content is decreased, these clouds are able to travel longer distances while for the last blend i.e. D50O50 they disappear before the other three blends.

From Fig. 15(a), the benefits of using high fractions of OME_x over soot formation are clear. However, it is convenient to compare them with certain disadvantages it could produce. As it has been mentioned previously, one of the main drawbacks is the energy reduction. For this purpose, the maximum net soot formed and the total energy released (TER) for each blend are summarized in Table 7. Besides, the percentage of variation of both parameters for each blend with respect to D90O10 has been also included.

The percentage of reduction of soot formation increases sharply when blend contains 70% or more OME_x in it. At first, it can be seen that there is almost no difference between D90O10 and D80O20, although, in comparison, the D50O50 blend produces almost 57% less soot than D90O10. However, when looking at the TER reduction, the variation is much lower. Between D90O10 and D50O50, only 15.6% of reduction was obtained. Thus, it can be concluded that reductions in soot formation of up to 50% would only require to modify injection strategy to compensate for a 15% of energy loss.

4. Conclusions

The aim of this work has been to deepen into understanding how the properties and the stoichiometry of OME_x affect the combustion process and pollutant formation of OME_x-fossil fuel blends in a CI engine when the composition is varied within a wide range (from 10 to 50% of OME_x content in the mixture). For this purpose, CFD simulations of a medium duty optical engine has been performed using n-heptane (Diesel) and OME_3 (OME_x) as surrogate fuels: Besides, experimental data obtained

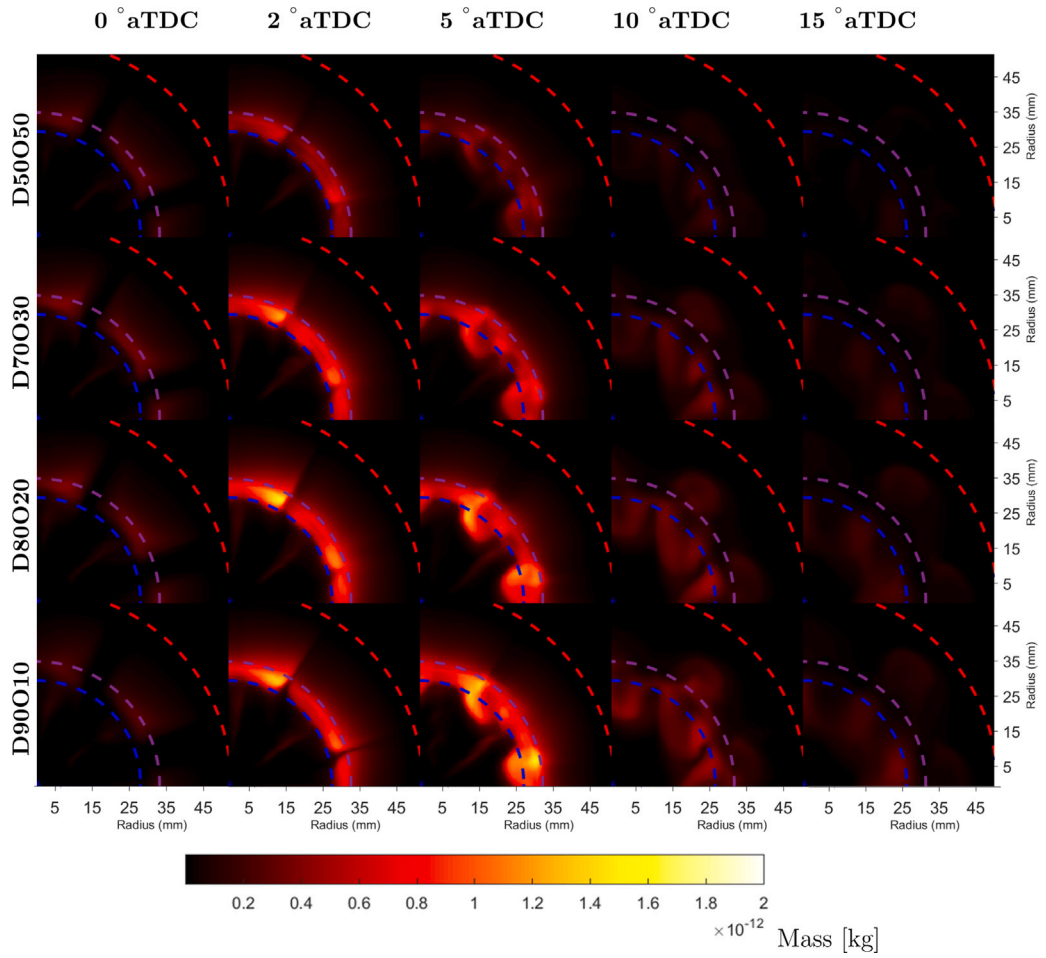

Fig. 16. Accumulated soot mass inside the combustion chamber. Data corresponds to numerical simulations.

Table 7
Total energy released (TER) reproduced from [12] and maximum net soot formed corresponding to numerical simulations for each blended fuel along with % variation of both parameters with respect to D90O10.

Blend	Total energy released (TER) (J)	Maximum net soot formed (mg)	% Decrease in total energy released	% Decrease in net soot formed
D50O50	1024.0	0.0139	15.56	56.8
D70O30	1096.6	0.0250	9.57	22.4
D80O20	1146.6	0.0305	5.45	5.3
D90O10	1217.7	0.0322	–	–

at the same optical engine has been used to corroborate the numerical results.

First, different reaction mechanism from literature were evaluated for these mixtures. The results showed that the most compact reaction mechanism provided by Lin 2019 [32] is able to reproduce a global combustion behaviour similar to the one observed with the experimental data. However, the other three mechanisms evaluated He 2017 [31], Ren 2019 [24], Lin 2021 [26] were providing larger ignition delays, which strongly affected the rest of the combustion process. Using the selected reaction mechanism, simulations of different blends of n-heptane and OME_3 were carried out. The main conclusions obtained from the analysis of the data obtained are summarized here:

- The ignition delay of the blend decreases when increasing the OME_3 content and the trend tends asymptotically to a value similar to that of D50O50. This suggest that above 20% OME_3, the ignition delay of these blends is mostly controlled by the most reactive component.
- The HRR at the premixed combustion phase increased when decreasing the OME_3 fraction, which can be related with the lower LHV of this fuel but also with the different ID of the blends. On the other hand, the HRR levels reached during the diffusion phase are more similar despite the difference in terms of LHV. In addition, it has been also observed at the late stages of combustion that an increase of OME_3 content also increases the combustion speed up to 5% for D50O50 when compared to D90O10.
- The different stoichiometry of OME_3 leads to a decrease of the Φ field. In this sense, D50O50 provides a different behaviour than the other blends. The fact that it reaches lower Φ values (closer to 1) is promoting oxidation reaction which result in a faster combustion completion and sooner OH disappearance.
- The higher Φ values reached when reducing the OME_3 content has been related with the higher net soot formation. On one hand, the soot formation increases as the amount of mixture under $\Phi > 2$ increases. On the other hand, the percentage of soot oxidation decreases too. This leads to a higher amount of soot in the cylinder, which lasts longer before being oxidized.

The numerical simulation highlights the benefits of using OME_3 when partially replacing fossil Diesel in CI engines. The lower LHV of the

fuel is a constraint but the faster oxidation process reported here would allow to increase injection duration to compensate for that. With low OME_3 percentages (below 20%) the soot decrease is not remarkable. However, for D70O30 and D50O50 more important differences were observed which is interesting to reduce the soot-NO_x trade-off in this type of engines. Besides, this effect is relatively more intense than other disadvantages like the TER loss caused by the lower LHV of this fuel. However, a deeper study would be recommended under different operating conditions (e.g., with EGR) to confirm this. Finally, it is worth mentioning that the results obtained with numerical simulations have been corroborated with experimental data obtained in the same optical engine.

CRediT authorship contribution statement

José M. García-Oliver: Conceptualization, Methodology. **Ricardo Novella:** Conceptualization, Methodology, Supervision. **Carlos Micó:** Writing – review & editing, Validation. **Usama Bin-Khalid:** Writing – original draft, Formal analysis, Software, Visualization.

Declaration of competing interest

The authors declare that they have no known competing financial interests or personal relationships that could have appeared to influence the work reported in this paper.

References

[1] García A, Monsalve-Serrano J, Sari RL, Martinez-Boggio S. Influence of environmental conditions in the battery thermal runaway process of different chemistries: Thermodynamic and optical assessment. Int J Heat Mass Transfer 2022;184:122381. http://dx.doi.org/10.1016/j.ijheatmasstransfer.2021.122381.

[2] García A, Monsalve-Serrano J, Sari RL, Tripathi S. Pathways to achieve future CO2 emission reduction targets for bus transit networks. Energy 2022;123177. http://dx.doi.org/10.1016/j.energy.2022.123177.

[3] Pastor JV, García A, Micó C, Lewiski F, Vassallo A, Pesce FC. Effect of a novel piston geometry on the combustion process of a light-duty compression ignition engine: An optical analysis. Energy 2021;221:119764. http://dx.doi.org/10.1016/j.energy.2021.119764.

[4] Deng W, Hu Q, Liu T, Wang X, Zhang Y, Song W, et al. Primary particulate emissions and secondary organic aerosol (SOA) formation from idling diesel vehicle exhaust in China. Sci Total Environ 2017;593:462–9. http://dx.doi.org/10.1016/j.scitotenv.2017.03.088.

[5] García A, Monsalve-Serrano J, Martínez-Boggio S, Wittek K. Potential of hybrid powertrains in a variable compression ratio downsized turbocharged VVA spark ignition engine. Energy 2020;195:117039. http://dx.doi.org/10.1016/j.energy.2020.117039.

[6] Pastor JV, García A, Micó C, Lewiski F. Simultaneous high-speed spectroscopy and 2-color pyrometry analysis in an optical compression ignition engine fueled with OMEX-diesel blends. Combust Flame 2021;230:111437. http://dx.doi.org/10.1016/j.combustflame.2021.111437.

[7] Chum HL, Overend RP. Biomass and renewable fuels. Fuel Process Technol 2001;71(1–3):187–95. http://dx.doi.org/10.1016/S0378-3820(01)00146-1.

[8] García A, Monsalve-Serrano J, Villalta D, Guzmán-Mendoza M. Parametric assessment of the effect of oxygenated low carbon fuels in a light-duty compression ignition engine. Fuel Process Technol 2022;229:107199. http://dx.doi.org/10.1016/j.fuproc.2022.107199.

[9] Grégoire L, Vincent F-L, Damien E, Christoph JM, Klaus SL. Electricity storage with liquid fuels in a zone powered by 100% variable renewables. In: 2015 12th international conference on the European energy market. IEEE; 2015, p. 1–5. http://dx.doi.org/10.1109/EEM.2015.7216634.

[10] He Y, Zhu L, Fan J, Li L, Liu G. Life cycle assessment of CO2 emission reduction potential of carbon capture and utilization for liquid fuel and power cogeneration. Fuel Process Technol 2021;221:106924. http://dx.doi.org/10.1016/j.fuproc.2021.106924.

[11] Pastor JV, García-Oliver JM, Micó C, García-Carrero AA, Gómez A. Experimental study of the effect of hydrotreated vegetable oil and oxymethylene ethers on main spray and combustion characteristics under engine combustion network spray A conditions. Appl Sci 2020;10(16):5460. http://dx.doi.org/10.3390/app10165460.

[12] Pastor JV, Garcia-Oliver JM, Micó C, Tejada FJ. Combustion behaviour of blends of synthetic fuels in an optical single cylinder engine. SAE Technical Papers, SAE International; 2021, http://dx.doi.org/10.4271/2021-24-0038.

[13] Zheng Y, Tang Q, Wang T, Liao Y, Wang J. Synthesis of a green fuel additive over cation resins. Chem Eng Technol 2013;36(11):1951–6. http://dx.doi.org/10.1002/ceat.201300360.

[14] Lumpp B, Rothe D, Pastötter C, Lämmermann R, Jacob E. Oxymethylene ethers as diesel fuel additives of the future. MTZ Worldw EMagazine 2011;72(3):34–8. http://dx.doi.org/10.1365/s38313-011-0027-z.

[15] Omari A, Heuser B, Pischinger S. Potential of oxymethylenether-diesel blends for ultra-low emission engines. Fuel 2017;209:232–7. http://dx.doi.org/10.1016/j.fuel.2017.07.107.

[16] García A, Monsalve-Serrano J, Villalta D, Sari RL, Zavaleta VG, Gaillard P. Potential of e-Fischer Tropsch diesel and oxymethyl-ether (OMEx) as fuels for the dual-mode dual-fuel concept. Appl Energy 2019;253:113622. http://dx.doi.org/10.1016/j.apenergy.2019.113622.

[17] Pastor JV, García A, Micó C, Lewiski F. An optical investigation of Fischer-Tropsch diesel and oxymethylene dimethyl ether impact on combustion process for CI engines. Appl Energy 2020;260:114238. http://dx.doi.org/10.1016/j.apenergy.2019.114238.

[18] Damyanov A, Hofmann P, Geringer B, Schwaiger N, Pichler T, Siebenhofer M. Biogenous ethers: Production and operation in a diesel engine. Automot Engine Technol 2018;3(1):69–82. http://dx.doi.org/10.1007/s41104-018-0028-x.

[19] Benajes J, García A, Monsalve-Serrano J, Martínez-Boggio S. Potential of using OMEx as substitute of diesel in the dual-fuel combustion mode to reduce the global CO2 emissions. Transp Eng 2020;1:100001. http://dx.doi.org/10.1016/j.treng.2020.01.001.

[20] Hank C, Lazar L, Mantei F, Ouda M, White RJ, Smolinka T, et al. Comparative well-to-wheel life cycle assessment of OME 3–5 synfuel production via the power-to-liquid pathway. Sustain Energy Fuels 2019;3(11):3219–33. http://dx.doi.org/10.1039/C9SE00658C.

[21] Novella R, García A, Pastor JM, Domenech V. The role of detailed chemical kinetics on CFD diesel spray ignition and combustion modelling. Math Comput Modelling 2011;54(7–8):1706–19. http://dx.doi.org/10.1016/j.mcm.2010.12.048.

[22] Sun W, Wang G, Li S, Zhang R, Yang B, Yang J, et al. Speciation and the laminar burning velocities of poly (oxymethylene) dimethyl ether 3 (POMDME3) flames: An experimental and modeling study. Proc Combust Inst 2017;36(1):1269–78. http://dx.doi.org/10.1016/j.proci.2016.05.058.

[23] He T, Wang Z, You X, Liu H, Wang Y, Li X, et al. A chemical kinetic mechanism for the low-and intermediate-temperature combustion of polyoxymethylene dimethyl ether 3 (PODE3). Fuel 2018;212:223–35. http://dx.doi.org/10.1016/j.fuel.2017.09.080.

[24] Ren S, Wang Z, Li B, Liu H, Wang J. Development of a reduced polyoxymethylene dimethyl ethers (PODEn) mechanism for engine applications. Fuel 2019;238:208–24. http://dx.doi.org/10.1016/j.fuel.2018.10.111.

[25] Lv D, Chen Y, Chen Y, Guo X, Chen H, Huang H. Development of a reduced diesel/PODEn mechanism for diesel engine application. Energy Convers Manage 2019;199:112070. http://dx.doi.org/10.1016/j.enconman.2019.112070.

[26] Lin Q, Tay KL, Zhao F, Yang W. Enabling robust simulation of polyoxymethylene dimethyl ether 3 (PODE3) combustion in engines. Int J Engine Res 2021;14680874211018363. http://dx.doi.org/10.1177/14680874211018363.

[27] Richards K, Senecal P, Pomraning E. Converge 3.0; convergent science: Madison, WI, USA. 2021.

[28] Payri F, Olmeda P, Martín J, García A. A complete 0D thermodynamic predictive model for direct injection diesel engines. Appl Energy 2011;88(12):4632–41. http://dx.doi.org/10.1016/j.apenergy.2011.06.005.

[29] Pitz WJ, Mueller CJ. Recent progress in the development of diesel surrogate fuels. Prog Energy Combust Sci 2011;37(3):330–50. http://dx.doi.org/10.1016/j.pecs.2010.06.004.

[30] Diez A, Crookes RJ, Løvås T. Experimental studies of autoignition and soot formation of diesel surrogate fuels. Proc Inst Mech Eng D 2013;227(5):656–64. http://dx.doi.org/10.1177/0954407012458402.

[31] He T, Liu H-y, Wang Y, Wang B, Liu H, Wang Z. Development of surrogate model for oxygenated wide-distillation fuel with polyoxymethylene dimethyl ether. SAE Int J Fuels Lubr 2017;10(3):803–14. http://dx.doi.org/10.4271/2017-01-2336.

[32] Lin Q, Tay KL, Zhou D, Yang W. Development of a compact and robust polyoxymethylene dimethyl ether 3 reaction mechanism for internal combustion engines. Energy Convers Manage 2019;185:35–43. http://dx.doi.org/10.1016/j.enconman.2019.02.007.

[33] Siebers DL. Scaling liquid-phase fuel penetration in diesel sprays based on mixing-limited vaporization. SAE Trans 1999;703–28. http://dx.doi.org/10.4271/1999-01-0528.

[34] Liu J, Sun P, Huang H, Meng J, Yao X. Experimental investigation on performance, combustion and emission characteristics of a common-rail diesel engine fueled with polyoxymethylene dimethyl ethers-diesel blends. Appl Energy 2017;202:527–36. http://dx.doi.org/10.1016/j.apenergy.2017.05.166.

[35] O'rourke P, Amsden A. A particle numerical model for wall film dynamics in port-injected engines. SAE Trans 1996;2000–13. http://dx.doi.org/10.4271/961961.

[36] Amsden AA, Findley M. KIVA-3V: A block-structured KIVA program for engines with vertical or canted valves. Tech. rep., Lawrence Livermore National Lab.(LLNL), Livermore, CA (United States); 1997, http://dx.doi.org/10.2172/505339.

[37] Issa RI. Solution of the implicitly discretised fluid flow equations by operator-splitting. J Comput Phys 1986;62(1):40–65. http://dx.doi.org/10.1016/0021-9991(86)90099-9.

[38] Senecal P, Pomraning E, Richards K, Briggs T, Choi C, McDavid R, et al. Multi-dimensional modeling of direct-injection diesel spray liquid length and flame lift-off length using CFD and parallel detailed chemistry. SAE Trans 2003;1331–51. http://dx.doi.org/10.4271/2003-01-1043.

[39] Hovden SL. Undersøkelse av reaksjonsmekanismer for OMEbrennstoff for bruk til implementering i 3D-CFD simulering av forbrenning. 2019, The University of Bergen, URL https://hdl.handle.net/1956/20495.

[40] Wang Z, Li L, Wang J, Reitz RD. Effect of biodiesel saturation on soot formation in diesel engines. Fuel 2016;175:240–8. http://dx.doi.org/10.1016/j.fuel.2016.02.048.

[41] Kitamura T, Ito T, Senda J, Fujimoto H. Mechanism of smokeless diesel combustion with oxygenated fuels based on the dependence of the equivalence ration and temperature on soot particle formation. Int J Engine Res 2002;3(4):223–48. http://dx.doi.org/10.1243/146808702762230923.